

Asymmetric Kelvin-Helmholtz instabilities in stratified shear flows

Adam J. K. Yang * and Mary-Louise Timmermans 

Department of Earth and Planetary Sciences, Yale University, New Haven, Connecticut 06511, USA

Gregory A. Lawrence 

*Department of Civil Engineering, University of British Columbia, Vancouver,
British Columbia V6T 1Z4, Canada*



(Received 11 September 2023; accepted 14 November 2023; published 2 January 2024)

In this study we explore the effect of an offset between the velocity and density interfaces on the dynamics and mixing of the Kelvin-Helmholtz (KH) instability in stratified shear flows. Most prior studies have assumed a coincident interface-symmetric KH instability. To investigate the asymmetric KH instability that emerges in the presence of offset interfaces, we conduct a linear stability analysis and direct numerical simulations, comparing results with the well-known symmetric KH instability. We find that the asymmetric KH instability is a hybrid mode of symmetric KH and Holmboe instabilities, with features of both overturning and scouring flows and a nonzero propagation speed. In contrast to the symmetric KH instability, the asymmetric KH instability does not generate a large-scale overturning of the central isopycnal but scours fluid of intermediate density from the upper portions of the interface, resulting in a significant interface deepening and sharpening of the density interface during mixing events. We observe that the dynamics and amount of mixing are strongly influenced by the degree of asymmetry (i.e., the offset distance between density and velocity interfaces) in the flow. With a larger asymmetry, the kinetic energy of the instability is larger but the cumulative mixing and mixing efficiency increase to a maximum then decrease. We find a similar transition of the gradient Richardson number distribution after the instabilities become turbulent, which has important implications for interpreting oceanographic data. Our study suggests that asymmetry should be taken into account in future studies of the KH instability.

DOI: [10.1103/PhysRevFluids.9.014501](https://doi.org/10.1103/PhysRevFluids.9.014501)

I. INTRODUCTION

Stably stratified shear flows play an important role in various contexts, such as estuaries [1], oceans [2], coastal inlets [3], ship canals [4], and lakes [5]. They are settings for stratified turbulent mixing, which transports tracers such as heat, salt, momentum, and biogeochemical substances. Understanding this mixing has broad applicability, ranging from predicting saltwater intrusion into estuaries to subgrid-scale parametrizations of property fluxes in general circulation models.

In a stably stratified system of layers separated by density interfaces, turbulent mixing occurs in intermittent and spatially inhomogeneous events driven by horizontal shear flow across the layers [6–8]. Studies have predominantly focused on the symmetric case in which the center of a velocity interface and a density interface coincide ($a^* = 0$, where a^* is the offset distance between the centers of the density and velocity interfaces; Fig. 1) and mixing events are modeled as the Kelvin-Helmholtz (KH) instability [9,10] or the Holmboe instability [11,12]. The KH instability

*jankang.yang@yale.edu

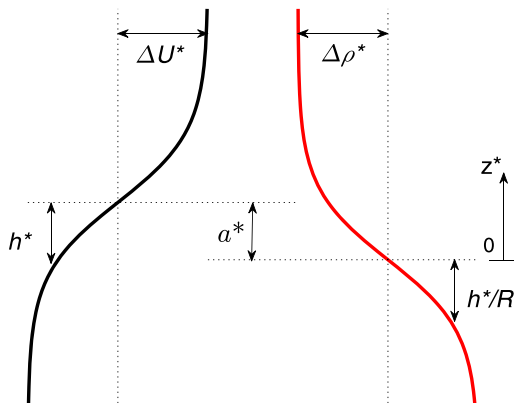


FIG. 1. Schematic illustrating the background fields of velocity (black) and density (red) of an asymmetric stratified shear layer. In the present study, the thickness of the velocity interface is the same as that of the density, $R = 1$.

occurs in flows where the velocity and density interface thicknesses are similar ($R \approx 1$, where R is the ratio of velocity to density interface thicknesses; Fig. 1) and is characterized by stationary overturns (or billows). The Holmboe instability occurs in flows where the density interface is thinner than the velocity interface and is characterized by propagating scouring waves; Alexakis [13] found that $R > 2$ is necessary for the Holmboe instability. Both types of instability have been commonly observed in natural settings.

Asymmetric profiles in which the velocity and density interfaces are offset from one another ($a^* \neq 0$; Fig. 1) are frequently encountered in geophysical flows in both laboratory experiments (e.g., [14–18]) and field observations (e.g., [1, 19–23]). This asymmetry may be due to topographic influences and forcing at a flow boundary (e.g., wind forcing on the surface of a water body or frictional processes at the bottom boundary). For example, Wesson and Gregg [19] observed prominent offsets between the density and velocity profiles in the Strait of Gibraltar (e.g., their Fig. 6). Asymmetric profiles have also been observed in the Fraser River estuary (see Fig. 5 of [1]), the Ishikari River estuary (Figs. 5 and 6 of [20]), and the Saint John River estuary (Fig. 9 of [21]). Therefore, it is natural to question how asymmetry affects the nonlinear evolution of instabilities and mixing in stratified shear flows.

Lawrence *et al.* [14] and Carpenter *et al.* [24] have demonstrated that introducing a vertical offset between the velocity and density interfaces when $R > 2$ (Fig. 1) results in an asymmetric Holmboe instability, which exhibits a mixture of KH and Holmboe instability characteristics in the linear normal-mode stability analysis. In laboratory experiments, velocity interfaces offset from thinner density interfaces lead to a one-sided flow with cusped waves and asymmetric billows that entrain fluid across the density interface [14]. This nonlinear evolution of asymmetric Holmboe instabilities was supported by direct numerical simulations focusing on the case $R = 3$ [24]; the evolution of the resultant instability depends on the degree of asymmetry in the background velocity and density profiles.

The effect of asymmetry with similar density and velocity interface thicknesses ($R = 1$), which exhibits significant differences in the results of linear stability theory and nonlinear simulations, remains largely unexplored. Recently, Olsthoorn *et al.* [25] tested the instability for $R = 1$ considering only a single value of asymmetry where the offset between the velocity and density interfaces is equal to half of the velocity interface thickness h^* ($a^* = h^*/2$). In this case the asymmetric KH instability arises and presents a hybrid instability sharing characteristics of both symmetric KH and Holmboe instabilities. However, the influence of the degree of asymmetry on the dynamics and mixing when $R = 1$ remains an open question and is the focus of this study.

In this paper we perform a set of three-dimensional direct numerical simulations with varying degrees of asymmetry (i.e., a range of a^*). The remainder of the paper is organized as follows. Section II describes the system setup, stability characteristics, numerical simulation methods, and framework by which the evolution of the flow is quantified. We then present the results of the three-dimensional simulations in Sec. III and explore the horizontally averaged flow evolution in Sec. IV. This is followed by the quantification of the influence of the asymmetry on the volume-averaged flow dynamics and mixing characteristics in Sec. V. Section VI presents the influence of asymmetry on marginal instability. A summary and discussion is given in Sec. VII.

II. METHODS

A. Setup

A density-stratified shear layer consists of initial velocity and density profiles whose variation in the vertical direction can be represented by hyperbolic tangent functions. The velocity distribution has a jump ΔU^* over a length scale h^* (Fig. 1). Similarly, the stable density distribution has a jump $\Delta \rho^*$ over a length scale h^* such that the velocity and density profiles are

$$\bar{U}^* = \Delta U^* \tanh\left(\frac{z^* - a^*}{h^*}\right), \quad (1)$$

$$\bar{\rho}^* = -\Delta \rho^* \tanh\left(\frac{z^*}{h^*}\right). \quad (2)$$

The velocity and density interface thicknesses are the same ($R = 1$), such that $h^* \equiv \Delta U^* / (d\bar{U}^*/dz^*)_{\max} \equiv \Delta \rho^* / (d\bar{\rho}^*/dz^*)_{\max}$. The center of the two interfaces are vertically offset by a^* (Fig. 1). The idealized hyperbolic tangent profiles have been used extensively in the literature (e.g., [8,26–29]), since they closely approximate the background profiles in many stratified flows in nature. Nondimensionalizing velocity by ΔU^* , density by $\Delta \rho^*$, and depth by h^* gives

$$\bar{U} = \tanh(z - a), \quad (3)$$

$$\bar{\rho} = -\tanh(z), \quad (4)$$

where dimensionless quantities are denoted without asterisks.

We define four dimensionless parameters that characterize the system: the Reynolds number (Re), the bulk Richardson number (Ri_b), the Schmidt number (Sc), and the asymmetry (a), given by

$$\text{Re} \equiv \frac{\Delta U^* h^*}{\nu^*}, \quad (5)$$

$$\text{Ri}_b \equiv \frac{\Delta \rho^* g^* h^*}{\rho_0^* (\Delta U^*)^2}, \quad (6)$$

$$\text{Sc} \equiv \frac{\nu^*}{D^*}, \quad (7)$$

$$a \equiv \frac{a^*}{h^*}, \quad (8)$$

where g^* is the gravitational acceleration, ρ_0^* is a reference density, ν^* is the kinematic viscosity, and D^* is the molecular diffusivity of the density field. Note that we define these dimensionless numbers based on the shear interface half-width and half-velocity difference, while in some studies the full scales are used (e.g., [24]). We use the same nondimensional parameters as those used by Olsthoorn *et al.* [25]: $\text{Re} = 1200$, $\text{Ri}_b = 0.15$, $\text{Sc} = 9$. These values ensure that the turbulence generated by the stratified shear instability reaches a buoyancy Reynolds number of $O(100)$, representative of a wide range of flows in estuaries, oceans, and lakes (e.g., [5,25,30,31]). The value of $\text{Ri}_b = 0.15$ is

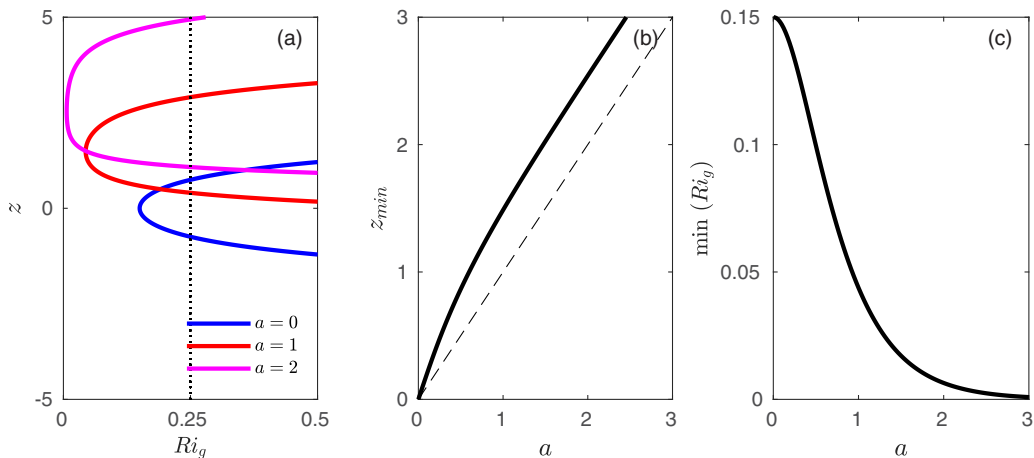


FIG. 2. (a) Profiles of Richardson number $Ri_g(z)$ for the hyperbolic tangent profiles shown in Fig. 1 with $Ri_b = 0.15$ and a variation of the degree of asymmetry a ; (b) the vertical level z_{min} of (c) the minimum value of Ri_g as function of a . The dotted vertical line in (a) indicates $Ri_g = 1/4$, and the dashed line in (b) indicates the 1:1 reference line.

representative of conditions found in both field and laboratory studies [32]. $Sc = 9$ corresponds to thermally stratified water with a temperature of approximately 12°C (Sc varies from 5.5 at 30°C to 13.1 at 0°C [33]). We further make this choice of Ri_b and Sc for comparison with previous studies that use the same (e.g., [24,25,34]). Hereafter, all quantities are dimensionless.

Variations in the degree of asymmetry, a , have significant influence on the stability of the flow. This is seen by considering the gradient Richardson number $Ri_g(z) = N^2/S^2$, where $N^2(z) = -Ri_b(d\bar{\rho}/dz)$ and $S^2 = (d\bar{u}/dz)^2$. By the Miles-Howard criterion, a necessary condition for instability (assuming inviscid parallel flow) is that $Ri_g(z) < 1/4$ at some level z [35,36]. For the hyperbolic tangent profiles used in this study, $Ri_g(z)$ attains a minimum in the region of the density interface [Fig. 2(a)]. For $a = 0$ (the symmetric case), the minimum is $Ri_g(z = 0) = Ri_b$. For $a > 0$ (asymmetry), the region where $Ri_g(z) < 1/4$ grows and shifts towards the center of the velocity interface [Figs. 2(a) and 2(b)]. This asymmetry also results in a lower minimum value [Fig. 2(c)] with minimum $Ri_g = Ri_b \operatorname{sech}^2(z_{min})/\operatorname{sech}^4(z_{min} - a)$ where $z_{min} = \{a + \sinh^{-1}[3 \sinh(a)]\}/2$, expressing the increased instability of the region above the density interface. For $R = 1$, this profile of $Ri_g(z)$ exhibits a fundamental difference from that for $R = 3$ (the Holmboe instability profile), which has $Ri_g(z) < 1/4$ located both above and below the center of the density interface [24].

The evolution of the velocity \mathbf{u} and density ρ are described by the nondimensional Navier-Stokes equations under the Boussinesq approximation:

$$\nabla \cdot \mathbf{u} = 0, \quad (9)$$

$$\frac{\partial \mathbf{u}}{\partial t} + \mathbf{u} \cdot \nabla \mathbf{u} = -\nabla p - Ri_b \rho \mathbf{k} + Re^{-1} \nabla^2 \mathbf{u}, \quad (10)$$

$$\frac{\partial \rho}{\partial t} + \mathbf{u} \cdot \nabla \rho = (Re Sc)^{-1} \nabla^2 \rho, \quad (11)$$

where p is the pressure and \mathbf{k} is the unit vector in the vertical direction.

B. Linear stability analysis

It is useful to examine the growth rate and length scales of the instability that determines the initial evolution via linear stability analysis. We solve the Navier-Stokes equations (9)–(11) based

on the assumptions of a parallel background mean flow and two-dimensional perturbations with normal mode forms (e.g., [16,37–39]). The velocity, pressure, and density fields are expressed in terms of the background field (denoted by overbars) plus a small perturbation (denoted by primes),

$$\mathbf{u} = \bar{U}(z)\mathbf{i} + \mathbf{u}'(x, z, t), \quad p = \bar{P}(z) + p'(x, z, t), \quad \rho = \bar{\rho}(z) + \rho'(x, z, t), \quad (12)$$

where the perturbations are much smaller than the background field (i.e., $|u'/\bar{U}| \ll 1$), and all perturbations have normal mode form

$$\psi'(x, z, t) \equiv \mathcal{R}\{\hat{\psi}(z)\exp(ikx + \sigma t)\}, \quad (13)$$

where \mathcal{R} denotes the real part; σ is the complex growth rate, k is the wave number, and \mathbf{i} is the unit vector in the horizontal direction.

Substituting these into the governing equations (9)–(11) yields

$$\sigma \begin{bmatrix} \nabla^2 & 0 \\ 0 & 1 \end{bmatrix} \begin{bmatrix} \hat{w} \\ \hat{\rho} \end{bmatrix} = \begin{bmatrix} \mathcal{L}_w & \mathcal{L}_{w\rho} \\ \mathcal{L}_{\rho w} & \mathcal{L}_\rho \end{bmatrix} \begin{bmatrix} \hat{w} \\ \hat{\rho} \end{bmatrix}, \quad (14)$$

where

$$\begin{aligned} \mathcal{L}_w &= -ik\bar{U}\nabla^2 + ik\frac{d^2\bar{U}}{dz^2} + \text{Re}^{-1}\nabla^4, \\ \mathcal{L}_\rho &= -ik\bar{U} + (\text{Re Sc})^{-1}\nabla^2, \\ \mathcal{L}_{w\rho} &= \text{Ri}_b \left(\frac{d^2}{dz^2} - \nabla^2 \right), \\ \mathcal{L}_{\rho w} &= -\frac{d\bar{\rho}}{dz}, \end{aligned} \quad (15)$$

and $\nabla^2 = -k^2 + d^2/dz^2$, $\nabla^4 = k^4 + d^4/dz^4 - 2k^2d^2/dz^2$. The streamwise velocity eigenfunction is then reduced to $\hat{u} = (i/k)\partial\hat{w}/\partial z$. The eigenvalue can be decomposed as $\sigma = \sigma_r + i\sigma_i$, where σ_r represents the growth rate of the instability and σ_i is related to the phase speed $c_p = -\sigma_i/k$. No-flux and free-slip boundary conditions are imposed at upper and lower boundaries.

Linear stability analysis indicates a continuous progression from the symmetric KH mode for $a = 0$ to an instability that appears closer to the Rayleigh instability (KH instability in a homogeneous fluid; Rayleigh [40]) for larger values of a (Fig. 3). Through the change from the symmetric KH instability to the Rayleigh instability, the maximum growth rate increases [Figs. 3(a) and 3(b)]. This is consistent with the vertical broadening of the region of $\text{Ri}_g(z) < 1/4$ and decrease of the minimal $\text{Ri}_g(z)$, lending a tendency to instability [Fig. 2(a)]. The wavelength of the maximum growth rate and its corresponding phase speed vary with a [Figs. 3(c) and 3(d)]. From $a = 0$ to $a \approx 1$, the most unstable wavelength decreases to reach a minimum while the phase speed increases to a maximum. With further increases in a above 1, the most unstable wavelength increases and the phase speed decreases. Only $a = 0$ exhibits zero phase speed, indicating the symmetric KH mode [41]; once $a > 0$, the phase speed is nonzero, indicating a hybrid mode of symmetric KH and Holmboe instabilities [Fig. 3(d)]. The phase speed returns to zero in the limit of large a . We will examine the nonlinear evolution including the transitional behavior in three-dimensional numerical simulations described next.

C. Numerical simulations

We performed three-dimensional direct numerical simulations (DNS) using the spectral parallel incompressible Navier-Stokes solver (SPINS), a parallelized pseudospectral solver [42], to solve the Navier-Stokes equations (9)–(11). The computational domain length $L_x = \lambda_x$ is set to the wavelength of the most unstable mode [varying slightly with the asymmetry; Fig. 3(c)]. The spanwise width of the domain is $L_y = 9$ ($> L_x/2$), which is sufficient for the development of

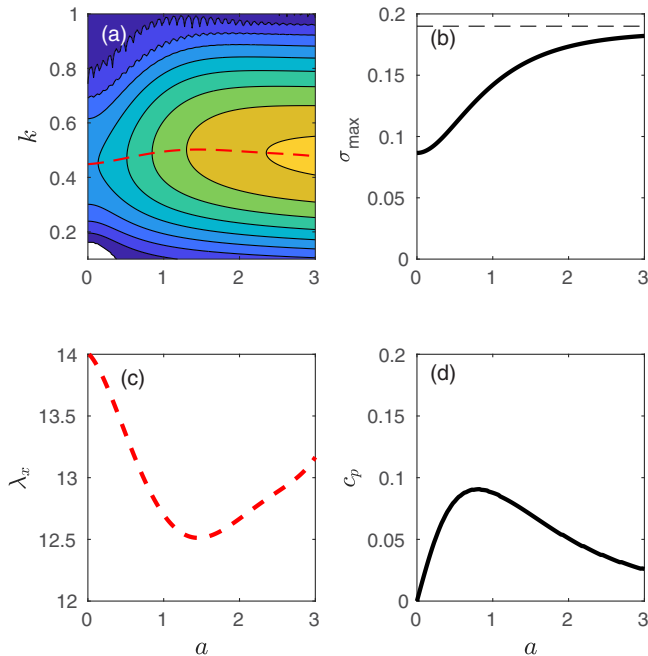


FIG. 3. Linear stability properties as a function of a of the unstable mode: (a) growth rate contours with the most unstable wave number (red dashed line); (b) maximum growth rate (thick line) and the fastest growth rate of the Rayleigh instability of an unstratified fluid (horizontal dashed line); (c) most unstable wavelength (used in setting the initial horizontal domain for the nonlinear numerical simulations); and (d) phase speed of the maximum growth rate. The values were obtained for the initial profiles in Fig. 1 with $Ri_b = 0.15$, $Re = 1200$, and $Sc = 9$.

three-dimensional secondary instabilities (e.g., [24,43]). The domain height $L_z = 18$ is large enough to have a negligible influence on the development of the instability (e.g., [25,44]). Periodic boundary conditions are imposed in the horizontal direction, and free-slip and no-flux boundary conditions are used in the vertical direction. $\{N_x, N_y, N_z\} = \{768, 512, 1024\}$ are the number of grid points in the horizontal, spanwise, and vertical directions, respectively. The suggested grid spacing in DNS is $O(L_K)$ where $L_K = (\nu^3/\varepsilon)^{1/4}$ is the Kolmogorov length scale and ε is the viscous dissipation rate [45,46]. However, in a stratified flow where $Sc > 1$, as is the case here, the required grid spacing needs to be $O(L_B)$, where $L_B = L_K/Sc^{1/2}$ is the Batchelor length scale. In our simulations, the computational resolution is $\sim 3L_B$ after the onset of turbulence (e.g., [24,25,47]).

Initial perturbations are applied to trigger instabilities (e.g., [25,34,47]). We use the eigenfunction of the fastest growing linear mode from the linear stability analysis (Sec. II B) and a random noise distribution. The amplitude of the eigenfunctions and the random noise are 1% and 0.1% of the background velocity difference, respectively.

We perform six different numerical experiments, exploring a range of asymmetry a between the initial velocity and density interfaces (Table I). Each of these simulations requires approximately 172 000 CPU hours. Note that in addition to the simulations with $Re = 1200$ and $Sc = 9$, we performed additional simulations with $Re = 300$ and $Sc = 1$ (see Appendix B).

D. Characterizing the partition and transfer of energy

To investigate the evolution of the flow through its various stages of development, it is useful to partition the energy into mean and perturbation parts. Following Caulfield and Peltier [43],

TABLE I. Summary of parameters for the numerical simulations. All simulations have $\text{Re} = 1200$, $\text{Ri}_b = 0.15$, and $\text{Sc} = 9$. The domain size is $\{L_x, L_y, L_z\}$, and the corresponding number of grid points used in each dimension is $\{N_x, N_y, N_z\} = \{768, 512, 1024\}$. The dimensionless maximum growth rate (σ_{\max}) and the corresponding phase speed (c_p) obtained from the linear stability analysis are given for each case.

Case no.	1	2	3	4	5	6
a	0	0.5	1.0	1.5	2.0	2.5
L_x	14.0	13.3	12.7	12.6	12.7	12.9
L_y	9	9	9	9	9	9
L_z	18	18	18	18	18	18
σ_{\max}	0.087	0.11	0.14	0.16	0.17	0.18
c_p	0	0.081	0.088	0.07	0.051	0.036

we decompose the velocity field, $\mathbf{u}(x, y, z, t)$, into the mean flow ($\bar{\mathbf{u}}$), the two-dimensional flow associated with the primary instability (\mathbf{u}_{2d}), and the three-dimensional flow (\mathbf{u}_{3d}):

$$\bar{\mathbf{u}} = \langle \mathbf{u} \rangle_{xy}, \quad (16)$$

$$\mathbf{u}_{2d} = \langle \mathbf{u} \rangle_y - \bar{\mathbf{u}}, \quad (17)$$

$$\mathbf{u}_{3d} = \mathbf{u} - \bar{\mathbf{u}} - \langle \mathbf{u} \rangle_{2d}, \quad (18)$$

where the subscript $\langle \cdot \rangle_i$ denotes averaging in the i direction. Similarly, we can decompose the kinetic energy ($K = \frac{1}{2} \langle \mathbf{u} \cdot \mathbf{u} \rangle_{xyz}$), into three components

$$K = K_{1d} + K_{2d} + K_{3d}, \quad (19)$$

where

$$K_{1d} = \langle \bar{\mathbf{u}} \cdot \bar{\mathbf{u}} \rangle_z, \quad (20)$$

$$K_{2d} = \langle \mathbf{u}_{2d} \cdot \mathbf{u}_{2d} \rangle_{xz}, \quad (21)$$

$$K_{3d} = \langle \mathbf{u}_{3d} \cdot \mathbf{u}_{3d} \rangle_{xyz}. \quad (22)$$

Following Lorenz [48] and Winters *et al.* [49], the irreversible time-dependent mixing rate is defined as

$$M \equiv dP_b/dt - \phi, \quad (23)$$

where $P_b = \text{Ri}_b \langle \rho_s z \rangle_z$ is the background potential energy obtained through a continuous adiabatic rearrangement of the instantaneous density field into a statically stable profile, $\rho_s(z)$, and $\phi = \text{Ri}_b (\bar{\rho}_{\text{bottom},t} - \bar{\rho}_{\text{top},t}) / (L_z \text{ReSc})$ is the mixing caused by molecular diffusion. Thus, M is equal to the instantaneous rate of monotonic increase in background potential energy after excluding the mixing caused by molecular diffusion and is always positive. The cumulative mixing is then given by

$$M_c = \int_0^t M dt = P_b(t) - P_b(0) - \phi t. \quad (24)$$

We use M to define a time-dependent instantaneous mixing efficiency as

$$E \equiv \frac{M}{M + \varepsilon}, \quad (25)$$

where $\varepsilon = \frac{2}{\text{Re}} \langle \mathbf{s}_{ij} \mathbf{s}_{ij} \rangle_{xyz}$ is the viscous dissipation rate of total kinetic energy and can be split into mean and fluctuating (turbulent) components, $\varepsilon = \langle \varepsilon \rangle + \varepsilon'$, where the mean is given by $\langle \varepsilon \rangle = \frac{1}{\text{Re}} \langle (\frac{d\bar{\mathbf{u}}}{dz})^2 \rangle_{xyz}$.

Finally, we define a cumulative mixing efficiency as

$$E_c \equiv \frac{\int_T M dt}{\int_T M dt + \int_T \varepsilon dt}, \quad (26)$$

where T denotes some duration of interest (e.g., [50]). Here T is the total duration of a mixing event between $t = 0$ and t_f where t_f is taken to be sufficiently long after the turbulent event (i.e., the flow has relaminarized) such that the result is insensitive to the exact value of t_f [24,25]; E_c gives the ratio of the energy used to perform mixing to the total energy expended in the mixing event. This gives an indication of the mixing efficiency of the entire event, rather than an instantaneous value.

III. THREE-DIMENSIONAL FLOW EVOLUTION

Our linear stability analysis indicates that the instability of the profiles, having $a > 0$ ($R = 1$), has characteristics of both symmetric KH and Holmboe instabilities. Here we describe DNS results showing that the mixed features of the linear stability lead to nonlinear flows that resemble both symmetric KH and Holmboe mixing events (Fig. 4).

For $a = 0$ (symmetric KH instability), the flow progresses in accordance with the usual evolution of a KH-driven mixing event [Figs. 4(a)–4(c); also see [51]]. Initially, the instability leads to the creation of the traditional billow structure with finite amplitude, overturning the stratified interface [Fig. 4(a)]. The primary growth is essentially two-dimensional and involves the entrainment of interfacial fluid into the core of the billow, which is stationary with respect to the mean flow and approximately symmetric vertically. Subsequently, the billow becomes unstable to three-dimensional secondary instabilities [Fig. 4(b)], triggering a transition to turbulence that fills the entire shear layer [Fig. 4(c)]. At the end of the simulation, the density interface is broader, with an almost equal mixture of the top and bottom fluid layers.

For $a = 1$ (asymmetric KH instability), the instability leads to the formation of a large billow, similar to the symmetric KH instability, but with some important differences [Figs. 4(d)–4(f)]. First, the size of the billow is larger compared to that of the symmetric KH instability. Second, the billow is positioned above the density interface and is not stationary with respect to the mean flow [i.e., has a nonzero phase speed as predicted by the linear stability analysis; Fig. 3(d)]. Third, the propagating billow scours fluid of intermediate density from the upper portions of the interface, which is different from the diffusive mixing of the symmetric KH instability. Secondary instabilities lead to three-dimensional motions in the billow, similar to the symmetric KH instability, but the resulting mixing is vertically asymmetric. The density gradient above the initial center of the density interface is mixed, and the density interface is sharpened while the fluid below the density interface remains largely intact [cf. Fig. 4(c) ($a = 0$) and Fig. 4(f) ($a = 1$)].

Further increasing the asymmetry ($a = 2$), the asymmetric KH instability forms an even larger billow [Fig. 4(g)]. The phase speed of the billow is smaller than for $a = 1$, consistent with the linear stability analysis [Fig. 3(d)]. With increasing degree of asymmetry, the resulting instability characteristics are reminiscent of the asymmetric Holmboe instability observed in laboratory experiments [18] and numerical simulations [24] at $\text{Re} = O(100)$; the billow behaves like a series of one-way ejections before decaying [24]. However, in our simulations with KH profiles ($R = 1$) at $\text{Re} = 1200$ these ejections are interrupted by the rapid formation of secondary instabilities [Fig. 4(h)]. The resulting mixing occurs primarily above the density interface, leading to an asymmetric final density interface with a larger vertical extent [Fig. 4(i)]. Three-dimensional motions mix only part of the initial interface, maintaining a strong density gradient on the lower side.

We next explore the details of the evolution of the interface for each of the cases ($a = 0, 1$ and 2) described here.

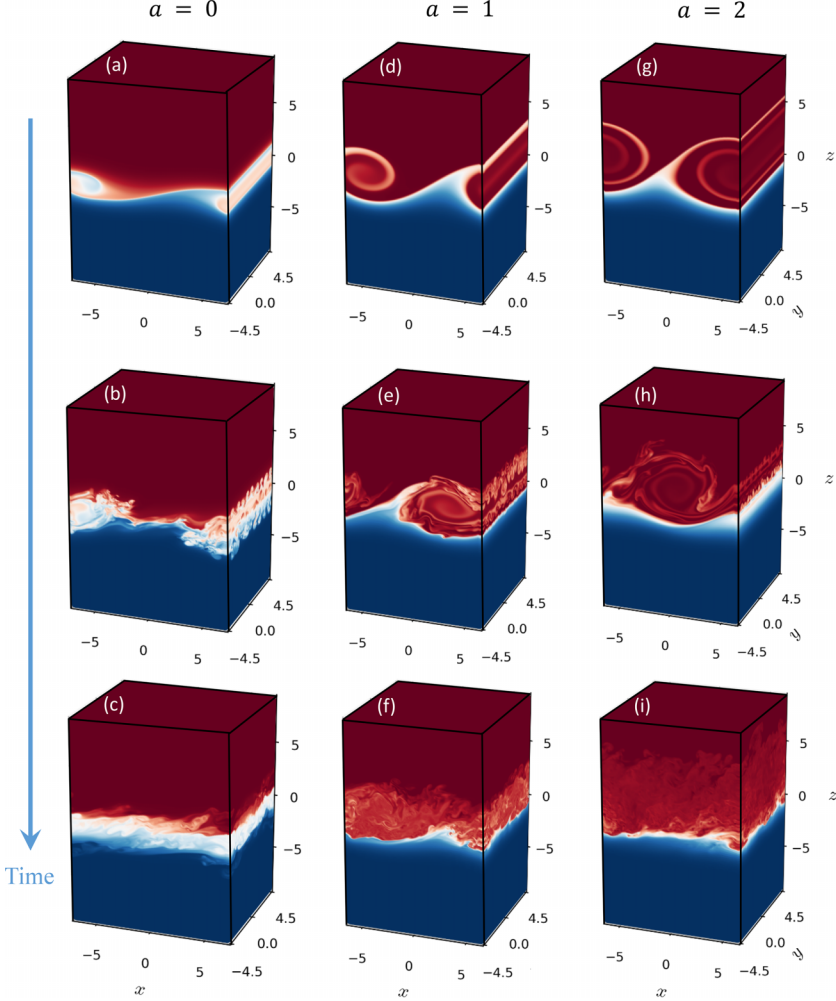


FIG. 4. Evolution of the three-dimensional density field at representative times (a)–(c) $a = 0$: $t = \{65, 110, 155\}$, (d)–(f) $a = 1$: $t = \{55, 110, 165\}$, and (g)–(i) $a = 2$: $t = \{50, 105, 160\}$.

IV. MIXING MECHANISMS

To better understand the spatio-temporal characteristics of the distinct mixing mechanisms related to the overturning of the symmetric KH and the scouring of the asymmetric KH instabilities, we explore the development of the horizontally averaged quantities (Fig. 5). We focus on horizontally averaged density profiles, buoyancy frequency ($\overline{N^2}$), dissipation rate ($\overline{\varepsilon}$), scalar variance dissipation rate ($\overline{\chi}$), and buoyancy Reynolds number ($\overline{\text{Re}_b}$):

$$\overline{N^2}(z, t) = -\text{Ri}_b \frac{d\overline{\rho}}{dz}, \quad \overline{\varepsilon}(z, t) = \frac{2}{\text{Re}} \overline{\mathbf{s}_{ij}\mathbf{s}_{ij}}, \quad \overline{\chi}(z, t) = \frac{2}{\text{Re Sc}} \overline{|\nabla\rho'|^2}, \quad \overline{\text{Re}_b}(z, t) = \frac{\overline{\varepsilon}}{\nu \overline{N^2}}, \quad (27)$$

where ρ' denotes the perturbation from the horizontally averaged mean density field $\overline{\rho}$.

The three-dimensional motion associated with the symmetric KH instability leads to symmetric disruption around the core of the initial density interface [Figs. 5(a)–5(e)] (see, e.g., [47]). The symmetry is seen in the spatial patterns of viscous and scalar dissipation [Figs. 5(c) and 5(d)]. On the other hand, the asymmetric KH instability results in a distinct one-sidedness, with greater mixing

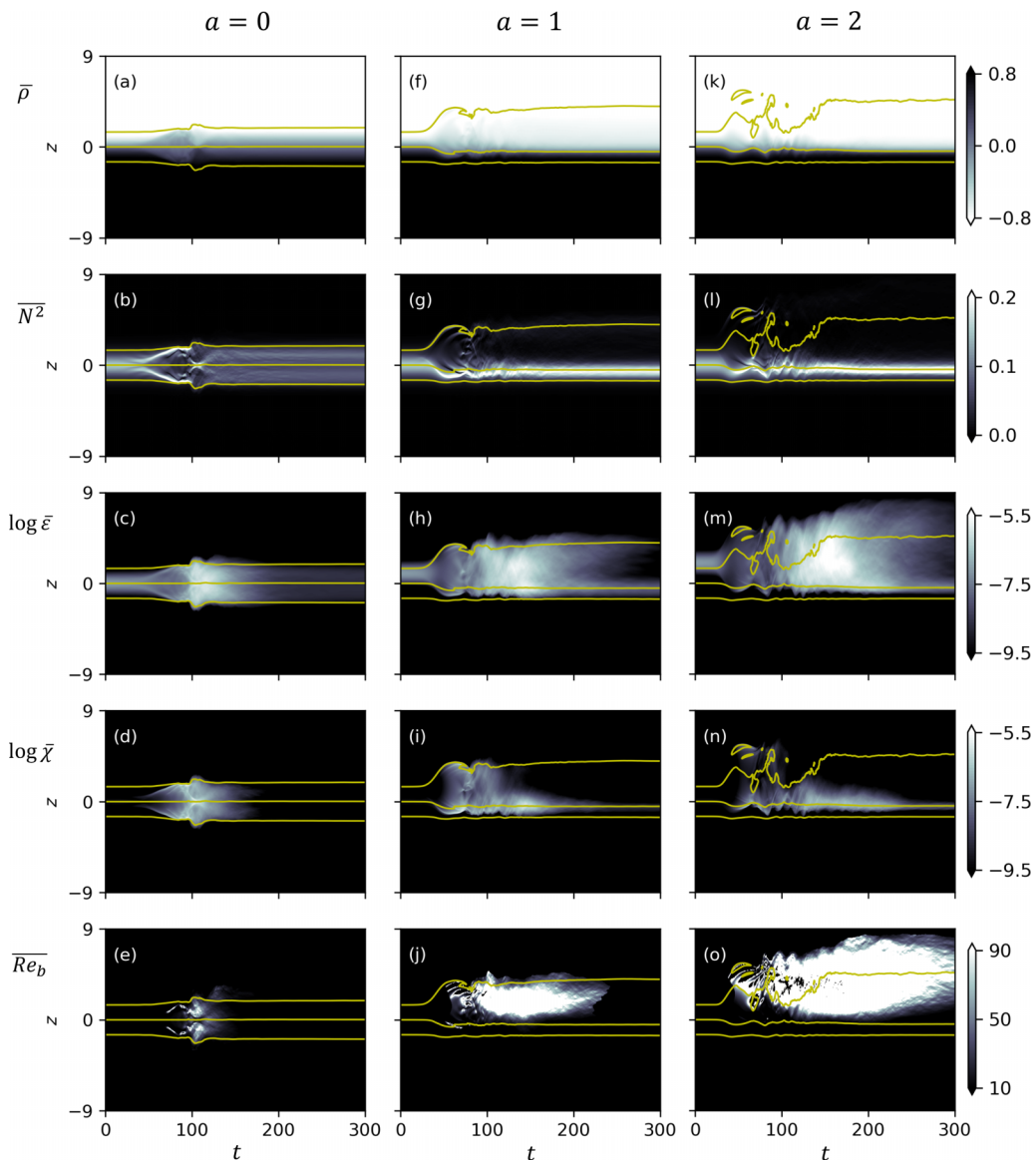


FIG. 5. Evolution of the horizontally averaged fields for $a = 0$ (left column), $a = 1$ (middle column), and $a = 2$ (right column). (a), (f), (k) density field, (b), (g), (l) $\overline{N^2}$, (c), (h), (m) $\log \bar{\epsilon}$, (d), (i), (n) $\log \bar{\chi}$, and (e), (j), (o) $\overline{Re_b}$. The base of the logarithms is e (natural logarithm). Superimposed on each plot are the $(-0.9, 0, 0.9)$ contours of the density field.

above the interface core than below [Figs. 5(f)–5(o) and 6(a)]. The dissipation and mixing due to viscosity occur mainly above the density interface, related to the breakdown of the initial billow structure [Figs. 5(h), 5(i), 5(m), and 5(n)]. With larger asymmetry, the strength of dissipation and mixing is larger. The symmetric KH instability has elevated values of Re_b throughout the density interface, while the asymmetric KH instability generates $Re_b = O(100)$ above the density interface [Figs. 5(e), 5(j), and 5(o)].

For $a > 0$, fluid from the lower layer is mixed into the upper layer in a scouring process [47]. Scouring results in a deepening and sharpening of the density interface defined by the position of

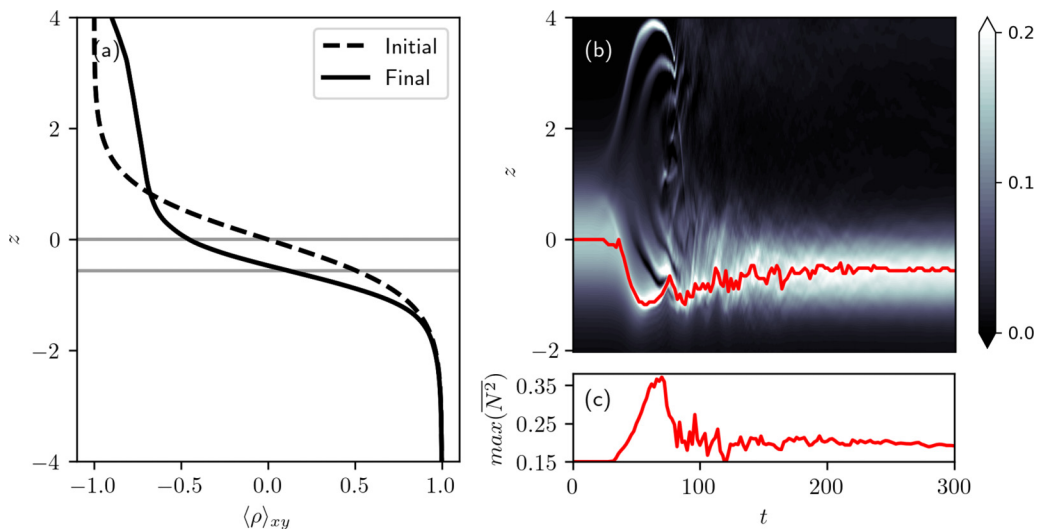


FIG. 6. Mixing due to the asymmetric KH instability for $a = 1$: (a) initial (dashed line) and final (solid line) density profiles with horizontal grey lines indicating the center of the density interface; (b) evolution of $\overline{N^2}$, where the location of the maximum $\overline{N^2}$ is indicated by the red line with its magnitude given in (c).

maximum horizontally averaged buoyancy frequency, $\overline{N^2}$ [Fig. 6(b)]. Below the density interface, the fluid layer remains unchanged. The scouring occurs immediately after the appearance of the KH billow with a significant initial interface deepening and sharpening [Fig. 6(b)]. After the billow breaks down ($t \approx 100$), there is some diffusive mixing across the interface and the stratification weakens (i.e., the interface broadens), while remaining more strongly stratified than its initial value.

With larger values of a (e.g., $a \geq 2$), the initial density interface is entirely below the shear interface. As a result, the instability growth is increasingly isolated from the density interface and the scouring becomes more intermittent. In the absence of active scouring, mixing across the interface is diffusive. In the later stages of the simulation, for the largest asymmetry, the stratification across the interface is weakest and its core is deepest because it is most diffusive; the diffusive mixing dominates over scouring. With a larger value of a , the instability is confined to a homogeneous layer with minimal cumulative mixing (and efficiency). We will quantify this next.

V. ENERGETICS AND MIXING

We quantify the volume average kinetic energy of the two-dimensional and three-dimensional motions in Sec. V A and the volume average turbulent dissipation, mixing rate and mixing efficiency in Sec. V B.

A. Kinetic energy

The two-dimensional kinetic energy (K_{2d}) increases most slowly as the instability grows for the symmetric cases ($a = 0$), with the fastest rate of increase when a is largest [Fig. 7(a)], consistent with the trend in growth rate predicted by the linear stability analysis [Fig. 3(b) and Table I]. This two-dimensional evolution relates to the growth rate of billow-like structures until K_{2d} reaches a maximum value at some time t_{2d} . After this time, K_{2d} exhibits oscillations as the transition to turbulence begins and the billow-like structures break down. Asymmetric cases ($a > 0$) have a higher kinetic energy associated with coherent billows compared to the symmetric case, with the most asymmetric case showing almost four times the peak energy as that of the symmetric KH instability [Fig. 7(a)]. Correspondingly, the most asymmetric case yields the strongest three-dimensional

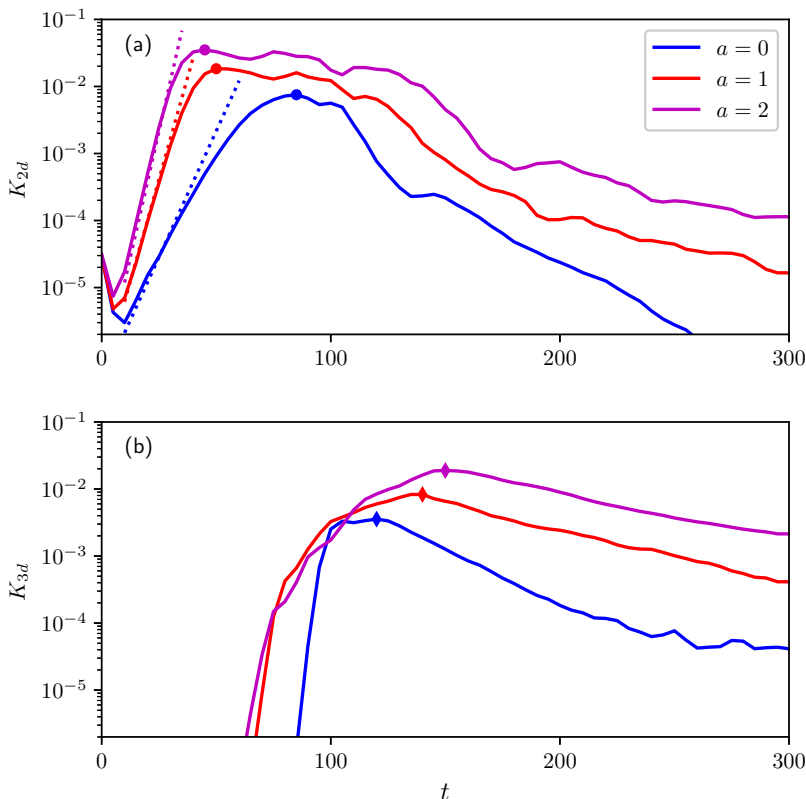


FIG. 7. Evolution of energy for $a = 0, 1$, and 2 : (a) two-dimensional kinetic energy (K_{2d}), and (b) three-dimensional kinetic energy (K_{3d}). In (a), the solid symbols indicate the time t_{2d} when K_{2d} is maximal for each case, and the dashed lines indicate the predicted growth rates from the linear stability analysis (see Table I). In (c), the solid symbols indicate t_{3d} when K_{3d} is maximal.

motion (K_{3d}) after the billow structure breaks down [Fig. 7(b)]. Interestingly, the time t_{3d} when K_{3d} is maximal is latest in the most asymmetric case [Fig. 7(b)], while t_{2d} is the earliest [Fig. 7(a)]; that is, the asymmetric KH instability is more long-lived with a larger degree of asymmetry. Note that it has been shown that t_{3d} could be influenced by the initial perturbation (see [52]). Therefore, the relationship between t_{3d} and a [Fig. 7(b)] might be qualitatively different for simulations with different initial perturbations.

B. Mixing

The temporal evolution of the turbulent dissipation rate ε' increases to a peak value corresponding with $t \approx t_{3d}$ and then decreases [Fig. 8(a)]. In agreement with the evolution of K_{3d} , ε' peaks at the latest time with the largest value for the most asymmetric case. Again, the asymmetric instability in this case is more long-lived and the size of billow is largest, thus the nonlinear evolution of the instability ensures the most energetic three-dimensional motions (see Appendix A). The mixing rate follows the same general evolution as the turbulent dissipation rate, with a stronger turbulent dissipation rate corresponding to a larger mixing rate [Fig. 8(b)]. Of note is that the mixing rate for asymmetric KH instabilities shows a double-peak pattern while the symmetric KH instability shows a single peak. The additional peak in the asymmetric cases originates from the nonzero phase speed which gives rise to an oscillation in the flow field. This is reminiscent of the oscillations in mixing

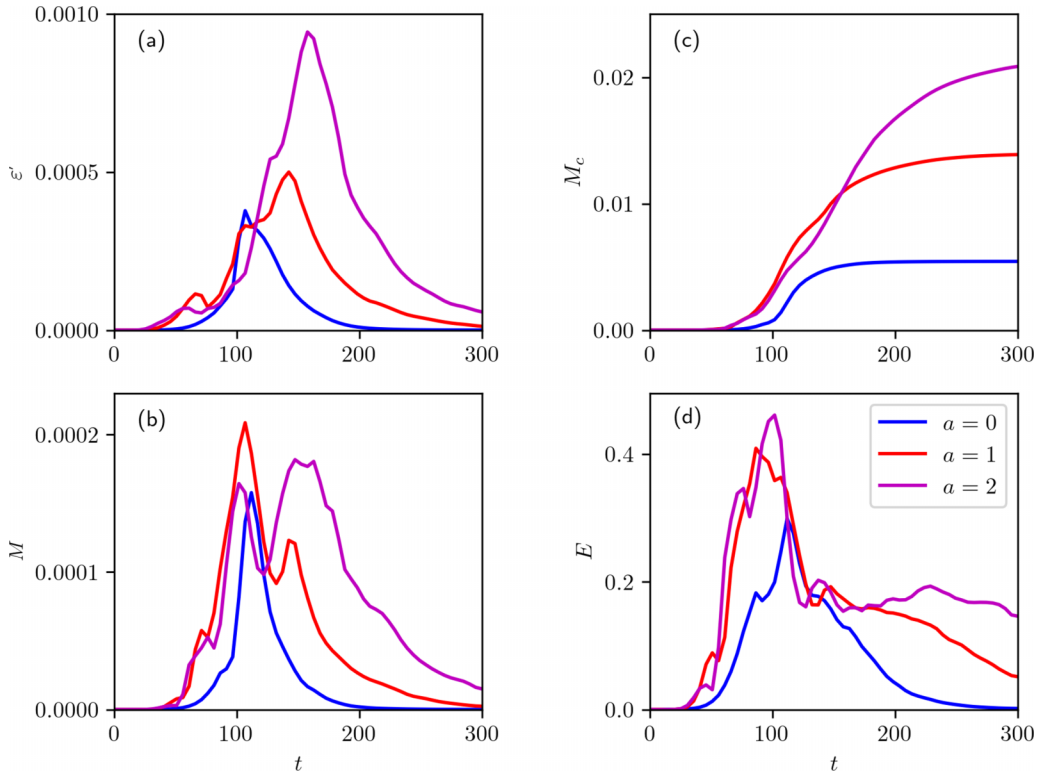


FIG. 8. Evolution of mixing parameters for $a = 0, 1$, and 2 : (a) turbulent dissipation rate, (b) mixing rate, (c) cumulative mixing, and (d) instantaneous mixing efficiency.

rate (associated with the propagation of the scouring wave) observed in the symmetric Holmboe mode before the instability breaks down (see [53]). Although all cases exhibit similar peak value in the mixing rate, with greater asymmetry, the mixing event lasts longer with a broader distribution of mixing over time. The three-dimensional motion is also more persistent, as shown by the larger cumulative mixing with greater asymmetry [Fig. 8(c)]. The instantaneous mixing efficiency peaks for asymmetric KH instabilities at $E \approx 0.4$ while that for symmetric KH instability is smaller at $E \approx 0.3$ during the flow transition, indicating a more efficient mixing induced by scouring than overturning events [i.e., $t < 150$; Fig. 8(d)]. After the flow becomes fully turbulent (i.e., $t > 150$), the mixing efficiency also follows the trend that larger asymmetry results in greater mixing efficiency.

Although an increased intensity of instantaneous dynamics and mixing is observed in cases of greater asymmetry, this does not necessarily lead to a greater mixing of the density field over the entire event. The dependence of the cumulative mixing and cumulative mixing efficiency on the degree of asymmetry is summarized in Fig. 9. For $a \lesssim 2$, larger values of a give rise to more cumulative mixing. For $a \gtrsim 2$, cumulative mixing decreases for larger a [Fig. 9(a)]. The overall cumulative mixing increases almost four times from the symmetric KH instability case to the asymmetric KH instabilities from $a = 0$ to $a = 2$. Although an increased billow size (thus an increased two-dimensional and three-dimensional energy) is observed in cases of greater asymmetry (Figs. 4 and 12), overturns do not mix fluid of different densities if they are not in contact with the density interface. The maximum value of the cumulative mixing as a function of a is an optimization between the size of the overturn and the area of fluid of different densities that is being mixed. When $a \gtrsim 2$ the initial velocity and density interfaces nearly no longer overlap, the scouring of fluid of different densities is not effective.

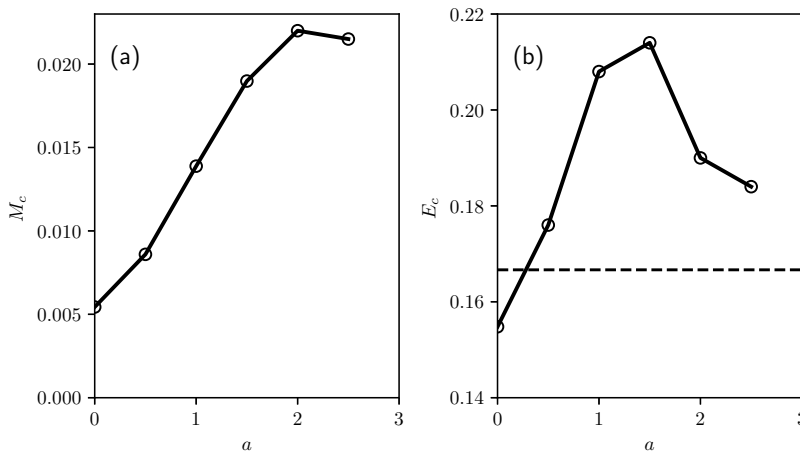


FIG. 9. Summary plots for each simulation showing the influence of the asymmetry on (a) cumulative mixing and (b) cumulative mixing efficiency for the entire event from $t = 0$ to t_f . The horizontal dashed line denotes the canonical $E_c = 1/6$ suggested by Osborn [54] for the average mixing efficiency of steady stratified shear flows. This value corresponds to a flux coefficient $\Gamma = E_c/(1 - E_c) = 0.2$.

Similarly, for $a < 2$, cumulative mixing efficiency is larger when a is larger [Fig. 9(b)]. Cumulative mixing efficiency peaks for values of $a \approx 1.5$ and drops off for larger values of a [Fig. 9(b)]. The overall cumulative mixing efficiency increases almost 40% from $a = 0$ to $a = 1.5$. Note that the computed cumulative mixing efficiency of the symmetric KH instability ($a = 0$) is close to the canonical value of $1/6$ suggested by Osborn [54] for steady stratified shear flows. This value is commonly used for mixing parametrizations although it has been a matter of some debate (e.g., [8,55,56]). Finally, the cumulative mixing efficiency peaks at a smaller a compared with that of the cumulative mixing. For larger a , although the cumulative mixing is larger, the cumulative dissipation rate is also larger, which gives rise to the decrease in the cumulative mixing efficiency [see Eq. (26)].

VI. MARGINAL INSTABILITY

Recent research has examined the concept of marginal instability in stratified turbulent flows, that is, the tendency for flows to evolve to a state with Ri_g near the critical value $1/4$ under background forcing (e.g., wind) [56–59]. Without background forcing, Salehipour *et al.* [60] found that marginal instability is present in symmetric Holmboe instabilities but not in symmetric KH instabilities. Marginal instability occurs through a continuously reinforced localization of scouring motions from symmetric Holmboe instabilities.

The symmetric KH instability has an initial state where Ri_g is minimal at the center of the velocity interface, while the asymmetric KH instabilities we study have minimal Ri_g above the center of the velocity interface (Fig. 10). With a larger a , the initial minimal Ri_g is smaller and the region where Ri_g is defined is broader in the vertical extent. After the instability grows and transitions to turbulence, the flow quickly evolves to a state approximating marginal instability. The asymmetric KH instability is characterized by lower values of Ri_g that persist for longer compared to the symmetric case. Increasing asymmetry delays the onset of turbulence, and the most asymmetric cases have the strongest three-dimensional motions in weakly stratified regions away from the density interface. The turbulent shear layer also exhibits a wider vertical extent of Ri_g , a manifestation of marginal instability. Throughout the scouring of asymmetric KH instabilities, both the density and velocity interfaces move downward with the latter at a faster rate [Figs. 10(b) and 10(c)]. As a result, the degree of asymmetry decreases, consistent with [25].

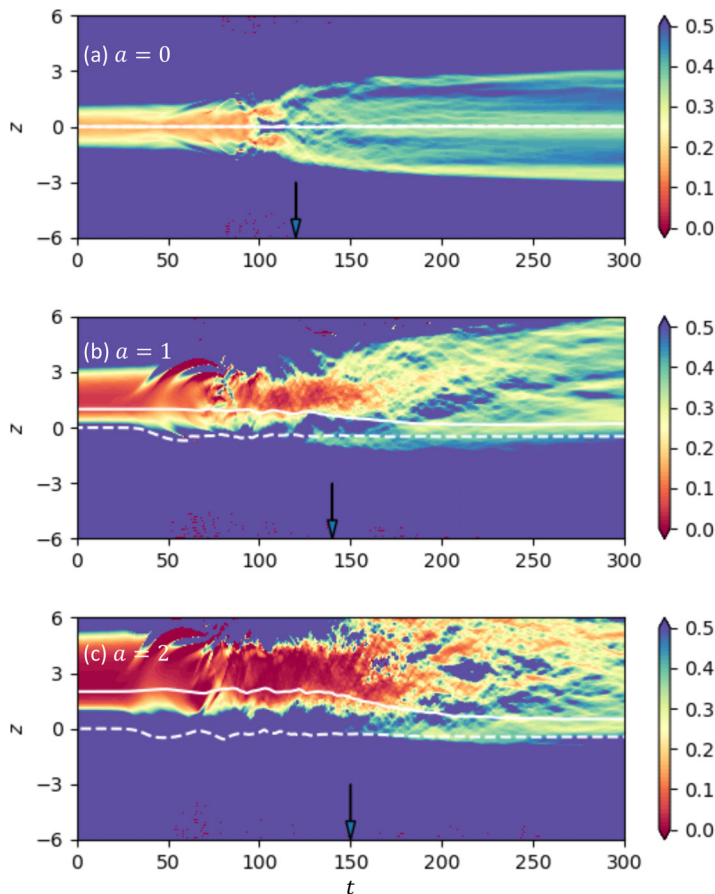


FIG. 10. Evolution of the horizontally averaged Ri_g for (a) $a = 0$, (b) $a = 1$, and (c) $a = 2$. The vertical arrow indicates $t = t_{3d}$; the white dashed and solid lines indicate the position of the density and velocity interfaces, respectively.

To quantify the distributions of gradient Richardson number, Ri_g , we computed the probability density function (PDF) of Ri_g within the turbulent region after time t_{3d} (labeled in Fig. 10). Following Olsthoorn *et al.* [25] and Salehipour *et al.* [60], we avoid values of Ri_g where both shear and stratification approach zero and include only sufficiently turbulent regions where dissipation rates satisfy $\varepsilon' > Sc\phi = \frac{2}{L_c} \frac{Ri_b}{Re}$. The PDF is strongly dependent on the degree of asymmetry which governs the KH-like versus Holmboe-like nature (Fig. 11). The PDF of the symmetric KH instability exhibits generally larger values (compared to the asymmetric case) and peaks of $Ri_g \approx 0.35$, consistent with the supercritical symmetric KH instability defined by Salehipour *et al.* [60]. Varying the asymmetry from $a = 0$ to 2, the location of the PDF peak decreases and approaches marginal instability as scouring becomes more prevalent; the PDF distribution becomes wider for larger a since the vertical extent over which Ri_g is defined is wider (see Fig. 10). However, the peak of the PDF shifts to larger Ri_g with further increases of a to 2.5. This transition is consistent with scouring being less effective when $a = 2.5$ [Fig. 9(a)]. It is interesting to note that the transition occurs at approximately $a = 2$ in the numerical simulations, while it occurs at approximately $a = 0.9$ in the linear stability analysis [Fig. 3(d)]. This discrepancy is presumably due to diffusion of background velocity and density in the nonlinear numerical simulations.

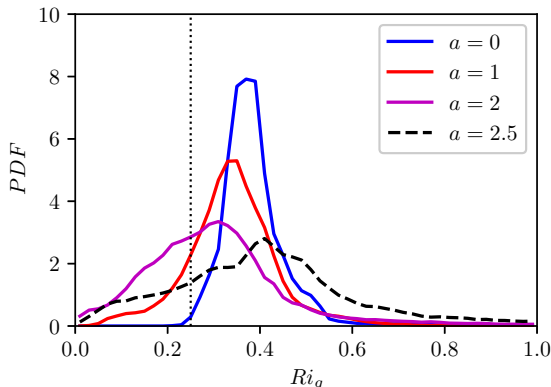


FIG. 11. Probability density function (PDF) of $Ri_g(z, t)$ for a range of asymmetries. The PDF is computed after the flow becomes turbulent ($t \geq t_{3d}$) and including only turbulent regions for which $\varepsilon' > \frac{2}{L_c} \frac{Ri_b}{Re}$ (see [25,60]). The vertical dotted line denotes $Ri_g = 1/4$.

VII. SUMMARY AND DISCUSSION

Most studies of the KH instability have focused on the scenario where the density and velocity interfaces are aligned. Here we studied the influence of an offset between the two interfaces to investigate the asymmetric KH instability, comparing results with the symmetric KH instability via linear stability analysis and DNS. Both linear stability analysis and DNS reveal that the asymmetric KH instability is a hybrid mode of symmetric KH and Holmboe instabilities (consistent with Olsthoorn *et al.* [25] with $a = 0.5$). The asymmetric KH instability exhibits longer maximal growth rates and a propagation with respect to the mean flow, which is evident in both the linear stability analysis and DNS. After the instability becomes turbulent, Ri_g approaches $1/4$, consistent with forcing and turbulent diffusion acting together to bring the mean flow to a state of marginal stability (e.g., [57]).

We have shown how the degree of asymmetry governs the dynamics and mixing associated with the instability. As the degree of asymmetry increases, the instability has a longer lifespan, and the associated two-dimensional kinetic energy is larger. Consequently, after the instability breaks, the three-dimensional kinetic energy and turbulent dissipation rate are also larger. On the other hand, the cumulative mixing and cumulative mixing efficiency are maximal for an asymmetry of $a \approx 2$ and drop off with further increases in asymmetry. The significance of $a = 2$ relates to the fact that at this asymmetry, the overlap between initial velocity and density interfaces is near minimal, and scouring of fluid of different densities is least effective. Note that this transition near $a = 2$ still holds for lower Re (i.e., for $Re = 300$ instead of 1200 ; see Appendix B 1).

The variation in mixing parameters for different degrees of asymmetry has important implications for estimating mixing in geophysical flows where asymmetry is commonly observed (e.g., see [1,19]). For example, assuming a mixing efficiency associated with the symmetric KH instability in a parametrization (e.g., [56]) may underestimate ocean mixing due to stratified turbulence by up to 40% (see Fig. 9). Future study is needed to quantify the influence of asymmetry for developing mixing parametrizations in terms of parameters such as the buoyancy Reynolds number [8]. The asymmetric KH instability may play an important role in wind-driven mixed layer deepening. The wind-forced Ekman layer at the ocean surface, where friction balances the Coriolis force, is often thinner than the mixed-layer, which is defined by a strong density gradient across its base (e.g., [61]). This sets up conditions for either the scouring asymmetric KH instability with a deepening density interface while the stratification remains strong, or ineffective mixing if the asymmetry is sufficiently large. Future field studies aimed at quantifying conditions during wind-driven mixed layer deepening are needed to explore the potential role of this mixing mechanism, and develop parametrizations for including this effect in models.

TABLE II. Summary of parameters for the numerical simulations (cases 7–14). All simulations have $Re = 300$ and $Ri_b = 0.15$. The domain size is $\{L_x, L_y, L_z\}$, and the corresponding number of grid points in each dimension is $\{N_x, N_y, N_z\} = \{256, 192, 384\}$ for cases 7–13. Case 14 has $\{N_x, N_y, N_z\} = \{512, 192, 384\}$, and accommodates two wavelengths of the fastest-growing instability. This case is run twice (14a and 14b), where the runs differ in their phase differences between initial perturbations (see Appendix B 2). The dimensionless maximum growth rate (σ_{\max}) and the corresponding phase speed (c_p) obtained from the linear stability analysis are given for each case.

Case no.	7	8	9	10	11	12	13	14
a	0	0.5	1.0	1.5	2.0	2.5	1.0	1.0
Sc	9	9	9	9	9	9	1	9
L_x	14.0	13.4	12.8	12.7	12.8	13.0	12.8	25.6
L_y	9	9	9	9	9	9	9	9
L_z	18	18	18	18	18	18	18	18
σ_{\max}	0.081	0.11	0.14	0.16	0.17	0.18	0.14	0.14
c_p	0	0.084	0.091	0.073	0.053	0.038	0.090	0.091

We note that while the simulations presented in this paper consider multiple values of Re and Sc , further exploration of the parameter space (Re , Ri_b , Sc , and R) would be of great value in understanding the role of asymmetry in stratified shear flows. For example, for asymmetric KH instability, the cumulative mixing and mixing efficiency associated with $Sc = 9$ is smaller than that with $Sc = 1$ (Appendix B 1). Understanding the mixing associated with larger Sc considering a salt stratification (for which Sc can be two orders of magnitude larger [33]) is important. In addition, we considered the case where the density and velocity interface thicknesses are equal ($R = 1$). Further study is needed to examine how mixing changes from KH profiles ($R = 1$) to Holmboe profiles ($R = 3$). Carpenter *et al.* [24] performed simulations to examine the influence of asymmetry for the case of $R = 3$ and $Re = 300$, lower than the value of $Re = 1200$ in our simulations; they found smaller cumulative mixing and mixing efficiency since the mixing was dominated by the quasilinear preturbulent stage of the instability. Additionally, for $R > \sqrt{2}$, the velocity (or density) interface core is the region of highest Ri_g (opposite to the case when $R < \sqrt{2}$, for which the core of the interface is the most unstable region characterized by a local minimum in Ri_g [34]). Despite these differences, the simulations of Carpenter *et al.* [24] show the same general relationships as in this study; they show cumulative mixing efficiency increases with asymmetry until the asymmetry is sufficiently large that the initial velocity and density interfaces are nearly no longer overlapped. Future studies are needed to explore how the dynamics and mixing of asymmetric instabilities change over a range of parameters Re , Ri_b , Sc , and R appropriate for environmental flows.

In symmetric shear instabilities, the interaction (or pairing) between adjacent vortices has been found to increase mixing (e.g., [51,52,62]). For asymmetric KH instability, we examined this effect via simulations with $Re = 300$, $Ri_b = 0.15$, $Sc = 9$, and $a = 1$; two simulations were run, each with different phase differences between the initial primary and subharmonic mode perturbations (see Table II). Vortex pairing is observed and the effect introduces more mixing just as in the symmetric case. Of note is that the effect of vortex pairing in asymmetric KH is insensitive to the phase difference between the initial perturbations, a result of the nonzero phase speed ([63] and Appendix B 2). Vortex pairing is not the only secondary instability that arises; a variety of three-dimensional secondary instabilities can also be present (see, for example, [64]). The particular secondary instabilities that dominate depend on the parameter regime as well as the initial perturbations. For Reynolds numbers of order 1000, Salehipour *et al.* [47] showed that increasing Re can enhance the growth of three-dimensional secondary instabilities which inhibit vortex pairing in the symmetric Holmboe instability. On the other hand, when asymmetry is large, the instability resembles the Rayleigh mode, and vortex pairing may potentially play an important role in scouring.

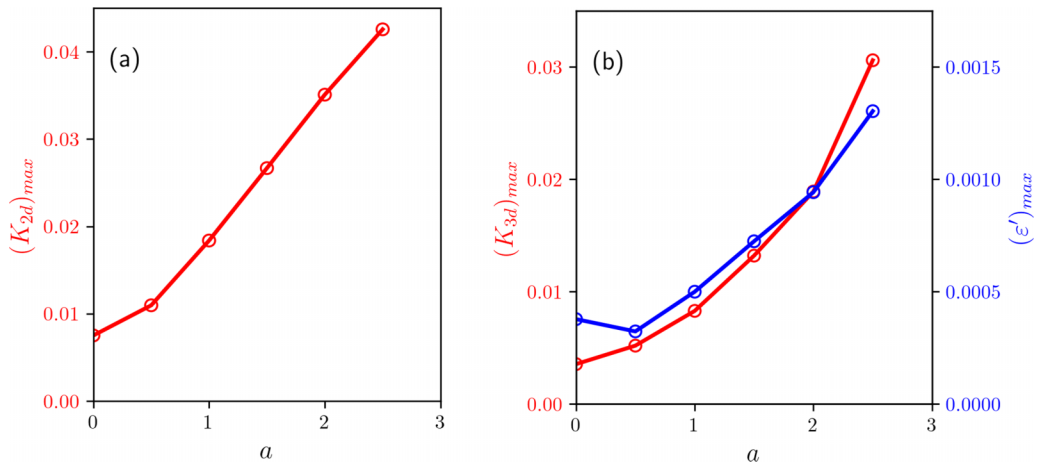


FIG. 12. Domain averaged kinetic energy as a function of the asymmetry on (a) the maximum 2D kinetic energy (K_{2d}) and (b) the maximum three-dimensional kinetic energy and its associated turbulent dissipation rate.

Further study is needed to examine the competition between vortex pairing and three-dimensional secondary instabilities in asymmetric KH for a range of Re , Ri_b , Sc , a , and initial perturbations.

ACKNOWLEDGMENTS

The authors acknowledge helpful discussions with J. Olsthoorn and helpful comments from two anonymous reviewers. A. J. K. Yang and M.-L. Timmermans were supported by funding from the Yale Center for Natural Carbon Capture. G. A. Lawrence was supported by the Natural Sciences and Engineering Research Council of Canada. We acknowledge high-performance computing support from the Yale Center for Research Computing.

APPENDIX A: MAXIMUM ENERGY

The dependence of the maximum two-dimensional kinetic energy (K_{2d}) shows that a larger asymmetry results in a larger peak value of K_{2d} , which relates to the size of the KH billow [Fig. 12(a)]. The size of a billow generated by the most asymmetric KH instability is approximately four times that of a billow generated by symmetric KH instability. When a larger billow breaks into three-dimensional flows, it produces stronger three-dimensional motions with a higher turbulent dissipation rate [Fig. 12(b)].

APPENDIX B: SIMULATIONS WITH $Re = 300$

Here we examine the mixing associated with asymmetric KH instabilities when $Re = 300$ (i.e., a lower value than the $Re = 1200$ simulations presented in the main text), and a range of asymmetry a (cases 7–12; Table II). We additionally examine a simulation with $Sc = 1$ (case 13; Table II) in Sec. B 1, and explore the influence of vortex pairing on mixing (via a larger horizontal domain, case 14; Table II) in Sec. B 2.

1. Cumulative mixing and mixing efficiency

The dependence of the cumulative mixing and cumulative mixing efficiency on the degree of asymmetry is summarized in Fig. 13. Similar to cases with $Re = 1200$ (Fig. 9), for $a \lesssim 2$, larger values of a give rise to more cumulative mixing and mixing efficiency (Fig. 13); for $a \gtrsim 2$,

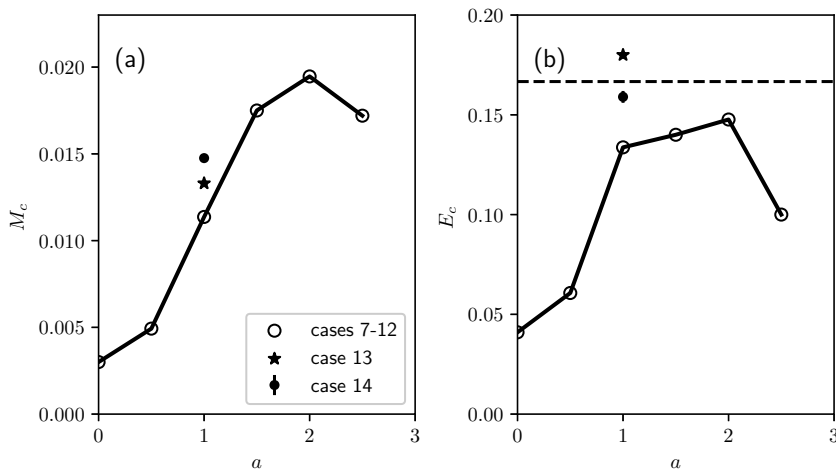


FIG. 13. Summary plots for the numerical simulations (cases 7–14). (a) Cumulative mixing and (b) cumulative mixing efficiency for the entire event from $t = 0$ to t_f . The insignificant error bar on the solid circle (case 14) indicates the negligible difference on mixing due to different phase differences between initial perturbations (see Appendix B 2). The horizontal dashed line denotes the canonical $E_c = 1/6$ suggested by Osborn [54] for the average mixing efficiency of steady stratified shear flows.

cumulative mixing and mixing efficiency decrease for larger a (Fig. 13). The overall cumulative mixing increases almost five times between the symmetric KH instability ($a = 0$) and the asymmetric KH instability with $a = 2$. When $a \gtrsim 2$ the overlap between initial velocity and density interfaces is near minimal, and scouring is not effective. Note that the cumulative mixing efficiency is smaller than the canonical $1/6$, since the mixing is dominated by the quasilinear preturbulent stage of the instability [24].

For a lower Schmidt number (Sc reduced from 9 to 1), the corresponding cumulative mixing and mixing efficiency increase (Fig. 13; case 13 has Sc = 1), consistent with results of the symmetric case [65]. Examining a range of Sc from 64 to 1 in three-dimensional simulations, Rahmani *et al.* [65] found that mixing induced by three-dimensional motions increases when Sc decreases. It is expected that the influence of Sc on mixing is similar for both the asymmetric and symmetric KH instabilities.

2. Influence of vortex pairing on mixing

To test the influence of vortex pairing on mixing, case 14 accommodates two wavelengths of the fastest-growing instability. This case is run twice (14a and 14b), where the runs differ in their phase differences between initial perturbations. Runs are initially perturbed by the eigenfunction corresponding to the KH and subharmonic modes from the linear stability analysis and random noise (see details in [62,63]). Similarly, we define the phase of each wave number mode in terms of two-dimensional vertical velocity, w_{2d} :

$$\theta_k = \frac{\pi}{2} + \arg\{\hat{w}_{2d,k}(z=0)\}, \quad (\text{B1})$$

where \arg is the argument of a complex number and $\hat{w}_{2d,k}$ is the k th Fourier component of the two-dimensional vertical velocity, and $k = 2$ corresponds to the KH mode and $k = 1$ corresponds to the subharmonic mode. The phase difference between the subharmonic mode and KH mode is denoted as

$$\theta_{\text{sub}} = \theta_1 - \theta_2. \quad (\text{B2})$$

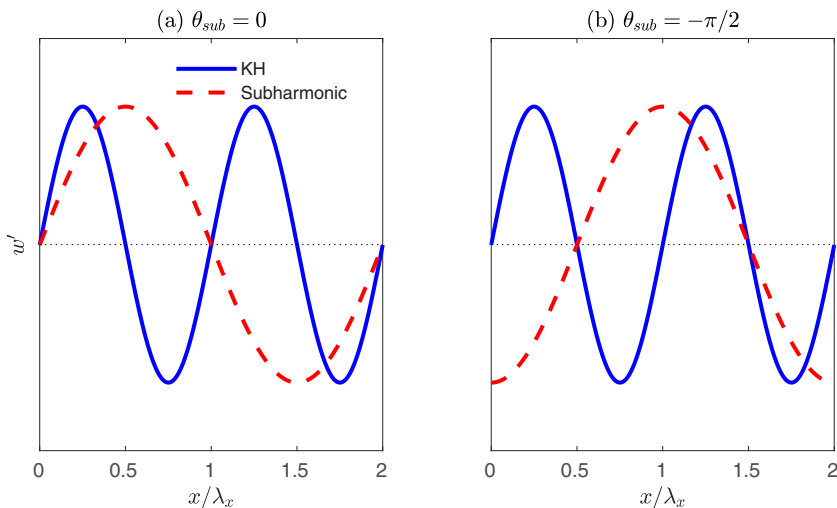


FIG. 14. Definition of the relative phase of the KH and subharmonic components based on $w'(z=0)$: (a) $\theta_{\text{sub}} = 0$ (case 14a) and (b) $\theta_{\text{sub}} = -\pi/2$ (case 14b).

Figure 14 illustrates the definition of the relative phase of the KH and subharmonic modes. Case 14 had initial perturbations with the relative phase $\theta_{\text{sub}} = 0$ (case 14a) and $\theta_{\text{sub}} = -\pi/2$ (case 14b). With initial perturbations of both the KH and subharmonic modes, Dong *et al.* [62] has shown that vortex pairing and the resultant mixing for the symmetric KH instability depend on θ_{sub} . When $\theta_{\text{sub}} = -\pi/2$, vortex pairing is inhibited in three-dimensional simulations and the associated mixing and mixing efficiency are minimal. When $\theta_{\text{sub}} = 0$, vortex pairing occurs and the associated mixing and mixing efficiency are maximal.

Vortex pairing for the asymmetric KH instability is illustrated in Fig. 15. For $\theta_{\text{sub}} = 0$, two rightward propagating asymmetric KH billows are observed at $t = 50$ [Fig. 15(a)]. As time

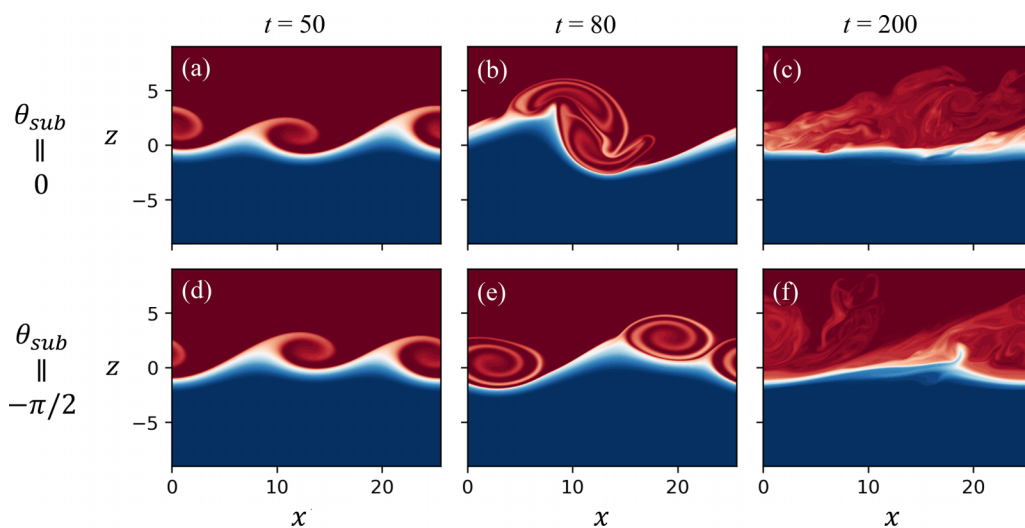


FIG. 15. Evolution of the density field ($x-z$) at representative times: (a)–(c) case 14a: $\theta_{\text{sub}} = 0$ and (d)–(f) case 14b: $\theta_{\text{sub}} = -\pi/2$.

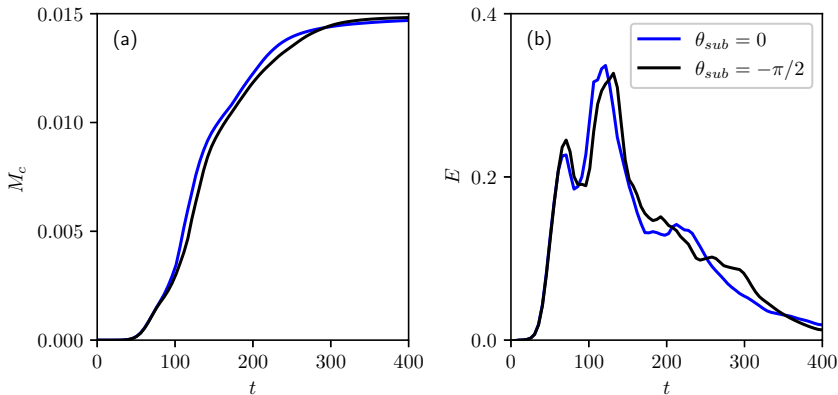


FIG. 16. Evolution of (a) cumulative mixing and (b) instantaneous mixing efficiency for case 14a with $\theta_{\text{sub}} = 0$ and case 14b with $\theta_{\text{sub}} = -\pi/2$.

progresses, the distance between them decreases. The vortex propagation speeds are different due to different amplitudes, resembling the vortex pairing in the symmetric Holmboe instability [63]. The two asymmetric KH billows undergo pairing [Fig. 15(d)], resulting in a larger billow before it breaks down [Fig. 15(c)]. The vortex pairing process for $\theta_{\text{sub}} = -\pi/2$ is slightly delayed compared with that for $\theta_{\text{sub}} = 0$.

The evolution of the mixing is insensitive to the phase difference θ_{sub} between the initial perturbations (Fig. 16), with the slight difference between simulations being a result of the time difference in the vortex pairing event. The cumulative mixing and mixing efficiency are higher in the presence of vortex pairing (Fig. 13). The insensitivity to the phase difference indicates that the vortex pairing process for the asymmetric KH instability is closer to that of the symmetric Holmboe instability rather than the symmetric KH instability. Due to the propagating nature of the asymmetric KH instability, the phase difference is adjusted during its initial linear development [63]. However, the symmetric KH instability is stationary, and thus the phase difference remains the same during the initial linear development period. A more comprehensive investigation, for example, using the combined effects of the initial perturbation amplitude ratio and relative phase, is the subject of a future study.

-
- [1] E. W. Tedford, J. R. Carpenter, R. Pawlowicz, R. Pieters, and G. A. Lawrence, Observation and analysis of shear instability in the Fraser River estuary, *J. Geophys. Res. Oceans* **114**, 2009JC005313 (2009).
 - [2] A. K. Kaminski, E. A. D’Asaro, A. Y. Shcherbina, and R. R. Harcourt, High-resolution observations of the North Pacific transition layer from a Lagrangian float, *J. Phys. Oceanogr.* **51**, 3163 (2021).
 - [3] D. Farmer and L. Armi, Stratified flow over topography: the role of small-scale entrainment and mixing in flow establishment, *Proc. R. Soc. Lond. Ser. A* **455**, 3221 (1999).
 - [4] G. A. Lawrence, R. Pieters, L. Zaremba, T. Tedford, L. Gu, S. Greco, and P. Hamblin, Summer exchange between Hamilton Harbour and Lake Ontario, *Deep Sea Res. Part II Top. Stud. Oceanogr.* **51**, 475 (2004).
 - [5] O. Sepúlveda Steiner, A. L. Forrest, J. B. McInerney, B. Fernández Castro, S. Lavanchy, A. Wüest, and D. Bouffard, Spatial variability of turbulent mixing from an underwater glider in a large, deep, stratified lake, *J. Geophys. Res. Oceans* **128**, e2022JC018913 (2023).
 - [6] F. S. Sherman, J. Imberger, and G. M. Corcos, Turbulence and mixing in stably stratified waters, *Annu. Rev. Fluid Mech.* **10**, 267 (1978).

- [7] G. N. Ivey, K. B. Winters, and J. R. Koseff, Density stratification, turbulence, but how much mixing? *Annu. Rev. Fluid Mech.* **40**, 169 (2008).
- [8] C. P. Caulfield, Layering, instabilities, and mixing in turbulent stratified flows, *Annu. Rev. Fluid Mech.* **53**, 113 (2021).
- [9] S. A. Thorpe, Experiments on the instability of stratified shear flows: Miscible fluids, *J. Fluid Mech.* **46**, 299 (1971).
- [10] W. D. Smyth and J. N. Moum, Ocean mixing by Kelvin-Helmholtz instability, *Oceanography* **25**, 140 (2012).
- [11] J. Holmboe, On the behavior of symmetric waves in stratified shear layers, *Geophys. Publ.* **24**, 67 (1962).
- [12] F. K. Browand and C. D. Winant, Laboratory observations of shear-layer instability in a stratified fluid, *Bound.-Layer Meteorol.* **5**, 67 (1973).
- [13] A. Alexakis, On Holmboe’s instability for smooth shear and density profiles, *Phys. Fluids* **17**, 084103 (2005).
- [14] G. A. Lawrence, F. K. Browand, and L. G. Redekopp, The stability of a sheared density interface, *Phys. Fluids* **3**, 2360 (1991).
- [15] N. Yonemitsu, G. E. Swaters, N. Rajaratnam, and G. A. Lawrence, Shear instabilities in arrested salt-wedge flows, *Dyn. Atmos. Oceans* **24**, 173 (1996).
- [16] A. Lefauve, J. L. Partridge, Q. Zhou, S. B. Dalziel, C. P. Caulfield, and P. F. Linden, The structure and origin of confined Holmboe waves, *J. Fluid Mech.* **848**, 508 (2018).
- [17] A. J. Yang, E. W. Tedford, and G. A. Lawrence, The spatial evolution of velocity and density profiles in an salt wedge, *Theor. Appl. Mech. Lett.* **9**, 403 (2019).
- [18] A. J. Yang, E. W. Tedford, J. Olsthoorn, and G. A. Lawrence, Asymmetric Holmboe instabilities in arrested salt-wedge flows, *Phys. Fluids* **34**, 036601 (2022).
- [19] J. C. Wesson and M. C. Gregg, Mixing at Camarinal sill in the Strait of Gibraltar, *J. Geophys. Res. Oceans* **99**, 9847 (1994).
- [20] S. Yoshida, M. Ohtani, S. Nishida, and P. F. Linden, Mixing processes in a highly stratified river, *Coast. Estuar. Stud.* **54**, 389 (1998).
- [21] N. C. Delpeche, T. Soomere, and M.-J. Lilover, Diapycnal mixing and internal waves in the Saint John River Estuary, New Brunswick, Canada with a discussion relative to the Baltic Sea, *Est. J. Eng.* **16**, 157 (2010).
- [22] H. van Haren, L. Gostiaux, E. Morozov, and R. Tarakanov, Extremely long Kelvin-Helmholtz billow trains in the Romanche fracture zone, *Geophys. Res. Lett.* **41**, 8445 (2014).
- [23] J. Tu, D. Fan, Q. Lian, Z. Liu, W. Liu, A. K. Kaminski, and W. D. Smyth, Acoustic observations of Kelvin-Helmholtz billows on an estuarine lutocline, *J. Geophys. Res. Oceans* **125**, e2019JC015383 (2020).
- [24] J. R. Carpenter, G. A. Lawrence, and W. D. Smyth, Evolution and mixing of asymmetric Holmboe instabilities, *J. Fluid Mech.* **582**, 103 (2007).
- [25] J. Olsthoorn, A. K. Kaminski, and D. M. Robb, Dynamics of asymmetric stratified shear instabilities, *Phys. Rev. Fluids* **8**, 024501 (2023).
- [26] P. Hazel, Numerical studies of the stability of inviscid stratified shear flows, *J. Fluid Mech.* **51**, 39 (1972).
- [27] J. S. Turner, *Buoyancy Effects in Fluids* (Cambridge University Press, Cambridge, 1979).
- [28] P. G. Drazin and W. H. Reid, *Hydrodynamic Stability* (Cambridge University Press, 2004).
- [29] W. D. Smyth and J. R. Carpenter, *Instability in Geophysical Flows* (Cambridge University Press, 2019).
- [30] S. G. Monismith, J. R. Koseff, and B. L. White, Mixing efficiency in the presence of stratification: When is it constant? *Geophys. Res. Lett.* **45**, 5627 (2018).
- [31] H. V. Dossier, M. Chanona, S. Waterman, N. C. Shibley, and M.-L. Timmermans, Changes in internal wave-driven mixing across the Arctic Ocean: Finescale estimates from an 18-year pan-Arctic record, *Geophys. Res. Lett.* **48**, e2020GL091747 (2021).
- [32] S. A. Thorpe, Laboratory observations of secondary structures in Kelvin-Helmholtz billows and consequences for ocean mixing, *Geophys. Astrophys. Fluid Dyn.* **34**, 175 (1985).
- [33] S. P. Haigh, Non-symmetric Holmboe waves, Ph.D. thesis, University of British Columbia, 1994.
- [34] W. D. Smyth and K. B. Winters, Turbulence and mixing in Holmboe waves, *J. Phys. Oceanogr.* **33**, 694 (2003).

- [35] L. N. Howard, Note on a paper of John W. Miles, *J. Fluid Mech.* **10**, 509 (1961).
- [36] J. W. Miles, On the stability of heterogeneous shear flows, *J. Fluid Mech.* **10**, 496 (1961).
- [37] D. Koppel, On the stability of flow of a thermally stratified fluid under the action of gravity, *J. Math. Phys.* **5**, 963 (1964).
- [38] K. M. Smith, C. P. Caulfield, and J. R. Taylor, Turbulence in forced stratified shear flows, *J. Fluid Mech.* **910**, A42 (2021).
- [39] A. J. Yang, E. W. Tedford, J. Olsthoorn, A. Lefauve, and G. A. Lawrence, Velocity perturbations and Reynolds stresses in Holmboe instabilities, *Phys. Fluids* **34**, 074110 (2022).
- [40] Lord Rayleigh, On the stability, or instability, of certain fluid motions, *Proc. Lond. Math. Soc.* **s1-11**, 57 (1880).
- [41] J. R. Carpenter, E. W. Tedford, E. Heifetz, and G. A. Lawrence, Instability in stratified shear flow: Review of a physical interpretation based on interacting waves, *Appl. Mech. Rev.* **64**, 060801 (2011).
- [42] C. J. Subich, K. G. Lamb, and M. Stastna, Simulation of the Navier-Stokes equations in three dimensions with a spectral collocation method, *Int. J. Numer. Methods Fluids* **73**, 103 (2013).
- [43] C. P. Caulfield and W. R. Peltier, The anatomy of the mixing transition in homogeneous and stratified free shear layers, *J. Fluid Mech.* **413**, 1 (2000).
- [44] S. P. Haigh and G. A. Lawrence, Symmetric and nonsymmetric Holmboe instabilities in an inviscid flow, *Phys. Fluids* **11**, 1459 (1999).
- [45] P. Moin and K. Mahesh, Direct numerical simulation: A tool in turbulence research, *Annu. Rev. Fluid Mech.* **30**, 539 (1998).
- [46] R. S. Arthur and O. B. Fringer, The dynamics of breaking internal solitary waves on slopes, *J. Fluid Mech.* **761**, 360 (2014).
- [47] H. Salehipour, C. P. Caulfield, and W. R. Peltier, Turbulent mixing due to the Holmboe wave instability at high Reynolds number, *J. Fluid Mech.* **803**, 591 (2016).
- [48] E. N. Lorenz, Available potential energy and the maintenance of the general circulation, *Tellus* **7**, 157 (1955).
- [49] K. B. Winters, P. N. Lombard, J. J. Riley, and E. A. D'Asaro, Available potential energy and mixing in density-stratified fluids, *J. Fluid Mech.* **289**, 115 (1995).
- [50] W. R. Peltier and C. P. Caulfield, Mixing efficiency in stratified shear flows, *Annu. Rev. Fluid Mech.* **35**, 135 (2003).
- [51] M. Rahmani, B. Seymour, and G. A. Lawrence, The evolution of large and small-scale structures in Kelvin–Helmholtz instabilities, *Environ. Fluid Mech.* **14**, 1275 (2014).
- [52] C.-L. Liu, A. K. Kaminski, and W. D. Smyth, The butterfly effect and the transition to turbulence in a stratified shear layer, *J. Fluid Mech.* **953**, A43 (2022).
- [53] W. D. Smyth, J. R. Carpenter, and G. A. Lawrence, Mixing in symmetric Holmboe waves, *J. Phys. Oceanogr.* **37**, 1566 (2007).
- [54] T. R. Osborn, Estimates of the local rate of vertical diffusion from dissipation measurements, *J. Phys. Oceanogr.* **10**, 83 (1980).
- [55] M. C. Gregg, E. A. D'Asaro, J. J. Riley, and E. Kunze, Mixing efficiency in the ocean, *Annu. Rev. Mar. Sci.* **10**, 443 (2018).
- [56] W. D. Smyth, Marginal instability and the efficiency of ocean mixing, *J. Phys. Oceanogr.* **50**, 2141 (2020).
- [57] S. A. Thorpe and Z. Liu, Marginal instability? *J. Phys. Oceanogr.* **39**, 2373 (2009).
- [58] W. D. Smyth, J. D. Nash, and J. N. Moum, Self-organized criticality in geophysical turbulence, *Sci. Rep.* **9**, 1 (2019).
- [59] M.-H. Chang, Marginal instability within internal solitary waves, *Geophys. Res. Lett.* **48**, e2021GL092616 (2021).
- [60] H. Salehipour, W. R. Peltier, and C. P. Caulfield, Self-organized criticality of turbulence in strongly stratified mixing layers, *J. Fluid Mech.* **856**, 228 (2018).
- [61] S. T. Cole, J. M. Toole, R. Lele, M.-L. Timmermans, S. G. Gallaher, T. P. Stanton, W. J. Shaw, B. Hwang, T. Maksym, J. P. Wilkinson *et al.*, Ice and ocean velocity in the Arctic marginal ice zone: Ice roughness and momentum transfer, *Elem. Sci. Anth.* **5**, 55 (2017).

- [62] W. Dong, E. W. Tedford, M. Rahmani, and G. A. Lawrence, Sensitivity of vortex pairing and mixing to initial perturbations in stratified shear flows, *Phys. Rev. Fluids* **4**, 063902 (2019).
- [63] A. J. K. Yang, E. W. Tedford, J. Olsthoorn, and G. A. Lawrence, Sensitivity of wave merging and mixing to initial perturbations in Holmboe instabilities, *Phys. Fluids* **34**, 126610 (2022).
- [64] A. Mashayek and W. R. Peltier, The ‘zoo’ of secondary instabilities precursory to stratified shear flow transition. Part 1 Shear aligned convection, pairing, and braid instabilities, *J. Fluid Mech.* **708**, 5 (2012).
- [65] M. Rahmani, B. R. Seymour, and G. A. Lawrence, The effect of Prandtl number on mixing in low Reynolds number Kelvin-Helmholtz billows, *Phys. Fluids* **28**, 054107 (2016).